

19. J. Dressel, Y. Choi, A. N. Jordan, *Phys. Rev. B* **85**, 045320 (2012).
20. F. Buscemi, P. Bordone, A. Bertoni, *Eur. Phys. J. D* **66**, 312–323 (2012).
21. E. Buks, R. Schuster, M. Heiblum, D. Mahalu, V. Umansky, *Nature* **391**, 871–874 (1998).
22. D. Sprinzak, E. Buks, M. Heiblum, H. Shtrikman, *Phys. Rev. Lett.* **84**, 5820–5823 (2000).
23. I. Neder, M. Heiblum, D. Mahalu, V. Umansky, *Phys. Rev. Lett.* **98**, 036803 (2007).
24. Y. Aharonov, D. Bohm, *Phys. Rev.* **115**, 485–491 (1959).
25. B. Rosenow, Y. Gefen, *Phys. Rev. Lett.* **108**, 256805 (2012).
26. A. Stern, Y. Aharonov, Y. Imry, *Phys. Rev. A* **41**, 3436–3448 (1990).
27. W. K. Wootters, W. H. Zurek, *Phys. Rev. D Part. Fields* **19**, 473–484 (1979).
28. G. Jaeger, A. Shimony, L. Vaidman, *Phys. Rev. A* **51**, 54–67 (1995).
29. B. G. Englert, *Phys. Rev. Lett.* **77**, 2154–2157 (1996).
30. I. Neder *et al.*, *Nature* **448**, 333–337 (2007).
31. J. Wheeler, W. Zurek, *Quantum Theory and Measurement* (Princeton Univ. Press, Princeton, NJ, 1983).
32. W. Chen *et al.*, *Phys. Rev. B* **87**, 155308 (2013).
33. A. A. Vyshnevyy, G. B. Lesovik, T. Jonckheere, T. Martin, *Phys. Rev. B* **87**, 165417 (2013).
34. V. Shpitalnik, Y. Gefen, A. Romito, *Phys. Rev. Lett.* **101**, 226802 (2008).
35. A. A. Vyshnevyy, A. V. Lebedev, G. B. Lesovik, G. Blatter, *Phys. Rev. B* **87**, 165302 (2013).

## ACKNOWLEDGMENTS

We thank K. Kang, Y. Chung, I. Neder, and H. Inoue for useful discussions. M.H. and Y.G. acknowledge the partial support of the

Israeli Science Foundation, the Minerva foundation, and the U.S.-Israel Binational Science Foundation (BSF). M.H. acknowledges also the support of the European Research Council under the European Community's Seventh Framework Program (FP7/2007-2013)/ERC grant agreement no. 227716, and the German Israeli Project Cooperation (DIP).

## SUPPLEMENTARY MATERIALS

[www.sciencemag.org/content/344/6190/1363/suppl/DC1](http://www.sciencemag.org/content/344/6190/1363/suppl/DC1)

Materials and Methods

Supplementary Text

Figs. S1 to S3

References (36, 37)

13 November 2013; accepted 23 May 2014

10.1126/science.1248459

## NANOMAGNETISM

# Nanoscale imaging and control of domain-wall hopping with a nitrogen-vacancy center microscope

J.-P. Tetienne,<sup>1,2</sup> T. Hingant,<sup>1,2</sup> J.-V. Kim,<sup>3</sup> L. Herrera Diez,<sup>3</sup> J.-P. Adam,<sup>3</sup> K. Garcia,<sup>3</sup> J.-F. Roch,<sup>1</sup> S. Rohart,<sup>4</sup> A. Thiaville,<sup>4</sup> D. Ravelosona,<sup>3</sup> V. Jacques<sup>1,2\*</sup>

The control of domain walls in magnetic wires underpins an emerging class of spintronic devices. Propagation of these walls in imperfect media requires defects that pin them to be characterized on the nanoscale. Using a magnetic microscope based on a single nitrogen-vacancy (NV) center in diamond, we report domain-wall imaging on a 1-nanometer-thick ferromagnetic nanowire and directly observe Barkhausen jumps between two pinning sites spaced 50 nanometers apart. We further demonstrate *in situ* laser control of these jumps, which allows us to drag the domain wall along the wire and map the pinning landscape. Our work demonstrates the potential of NV microscopy to study magnetic nano-objects in complex media, whereas controlling domain walls with laser light may find an application in spintronic devices.

Magnetic domain walls (DWs) represent nanoscale objects that form the cornerstone of a number of emerging spintronic applications, such as the racetrack memory (1), the magnetic random access memory (2), or the magnetic memristor (3). In such schemes, precise control of the positioning and motion of a single DW or a sequence of DWs along a track is paramount for their operation (4). However, in materials important for technology, such as ultrathin films with perpendicular magnetic anisotropy (5), defects can result in considerable pinning that impedes wall propagation. This pinning effect has two important consequences. First, it introduces a stochastic component into the

wall dynamics, whereby thermally driven processes involving hopping over energy barriers, or Barkhausen jumps, become important. Second, these processes can involve deformations in the DW profile itself, resulting in more complex two-dimensional (2D) dynamics such as creep in the low-velocity regime (6, 7). It is therefore an important challenge to quantify these aspects experimentally for realistic sample geometries.

The capacity to directly image DWs in nanostructures would provide valuable insight into how the structure of a DW deforms as it navigates through a complex energy landscape shaped by a random network of material defects. However, experimental techniques that allow this for practical spintronic devices with the requisite nanoscale spatial resolution are scarce. Techniques based on x-ray (8) or electron (9) microscopy, for example, suffer from a lack of signal because of the small interaction volumes in nanometer-thick films, whereas magnetic force microscopy is usually not suitable because DWs in ultrathin films are highly sensitive to magnetic perturbations. Other techniques, such

as spin-polarized scanning tunneling microscopy (10) and spin-polarized low-energy electron microscopy (11), can provide sufficient resolution to image wall structures but are limited to model systems.

Over the past few years, scanning nitrogen-vacancy (NV) center microscopy has emerged as a powerful magnetic imaging technique that provides quantitative measurements of the stray magnetic field emanating from a micromagnetic structure (12–16). This method is highly sensitive (17), produces no detectable magnetic backaction on the sample, and allows for a spatial resolution ultimately limited by the atomic size of the probe. This technique recently enabled stray-field imaging of a single electron spin (18) and of the vortex core in a magnetic microdot (19, 20). Here, we use scanning NV center microscopy to image, study, and control DWs in perpendicularly magnetized ultrathin wires.

The scanning NV center microscope employs the electronic spin of a single NV defect hosted in a diamond nanocrystal, which is attached to the tip of an atomic force microscope (21) and used as a magnetic field sensor (Fig. 1A). The magnetic field is evaluated within an atomic-size detection volume by encoding Zeeman shifts of the electron spin sublevels onto the spin-dependent photoluminescence (PL) intensity of the NV defect (16). To this end, a laser beam at the wavelength  $\lambda = 532$  nm is tightly focused onto the NV defect with a high-numerical aperture microscope objective, whereas a radiofrequency source allows for manipulation of its electron spin state. The spin-dependent red PL intensity of the NV defect is collected by the same objective and forms the magnetometer signal, which gives information about the projection  $|B_{NV}|$  of the local magnetic field along the NV center's quantization axis  $u_{NV}$  (Fig. 1A) (19, 22).

We studied a 1.5- $\mu$ m-wide Ta/CoFeB(1 nm)/MgO wire that exhibits perpendicular magnetic anisotropy (Fig. 1B). After preparing well-isolated DWs by applying short magnetic field pulses (22), the stray magnetic field was measured while operating the scanning NV center microscope in the “dual iso-B” imaging mode, which provides two different iso-magnetic field (iso-B) contours (19, 21). Figure 1C shows a typical magnetic field map

<sup>1</sup>Laboratoire Aimé Cotton, CNRS, Université Paris-Sud and ENS Cachan, UPR CNRS 3321, 91405 Orsay, France.

<sup>2</sup>Laboratoire de Photonique Quantique et Moléculaire, ENS Cachan and CNRS, UMR CNRS 8537, 94235 Cachan, France.

<sup>3</sup>Institut d'Electronique Fondamentale, Université Paris-Sud and CNRS, UMR CNRS 8622, 91405 Orsay, France.

<sup>4</sup>Laboratoire de Physique des Solides, Université Paris-Sud and CNRS, UMR CNRS 8502, 91405 Orsay, France.

\*Corresponding author. E-mail: [vjacques@ens-cachan.fr](mailto:vjacques@ens-cachan.fr)

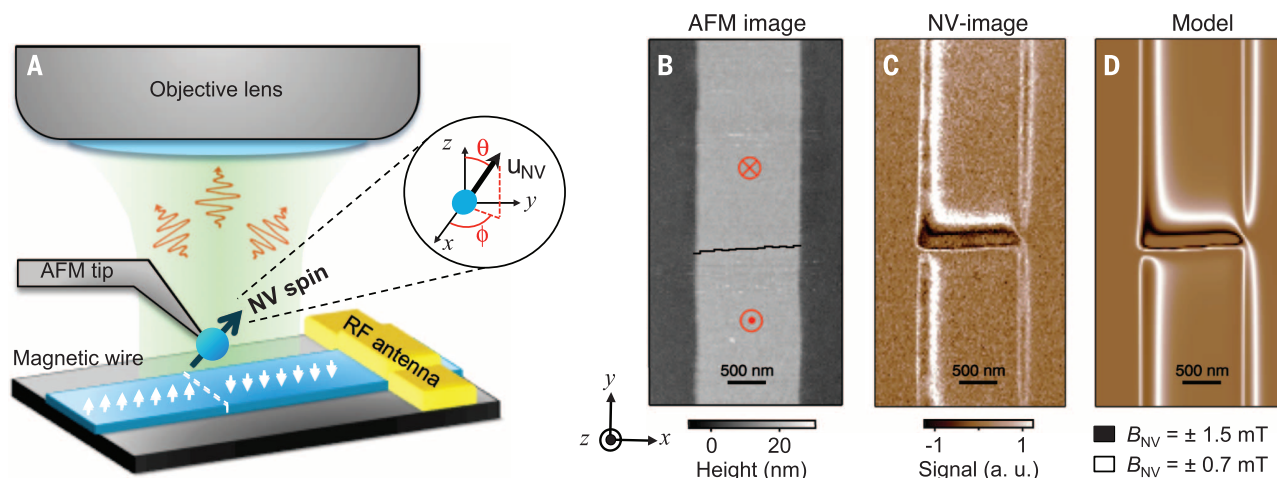


**Fig. 1. Imaging a DW in a 1-nm-thick magnetic wire.** (A) Schematic of the experimental setup. Magnetic field measurements are performed by a single NV defect placed at the apex of an atomic force microscope tip. The quantization axis  $u_{\text{NV}}$  of the NV defect used in this work is characterized by spherical angles  $\theta = 122^\circ$  and  $\phi = 45^\circ$ . RF, radiofrequency. (B) AFM image of the magnetic sample, a 1.5- $\mu\text{m}$ -wide Ta/CoFeB(1 nm)/MgO wire. The red symbols indicate the magnetization direction. (C) Dual iso-B image recorded

above the magnetic wire, revealing a single DW. Positive magnetometer signal (bright) indicates  $B_{\text{NV}} = \pm 0.7$  mT, whereas negative magnetometer signal (dark) indicates  $B_{\text{NV}} = \pm 1.5$  mT. a. u., arbitrary units. (D) Data fitting with micromagnetic calculations (22). The resulting DW profile is shown in (B) as a black line overlaid on the AFM image. In these experiments, the probe-sample distance is  $\approx 110$  nm, with the magnetic layer buried 7 nm below the sample surface. The acquisition time is 50 ms per pixel.

above the wire, with iso-B contours corresponding to  $B_{\text{NV}} = \pm 0.7$  and  $\pm 1.5$  mT. The field exhibits local maxima above the edges of the wire, but also along a line across the wire: this is the signature of a single DW. In such perpendicularly magnetized samples, the stray field is generated near regions of abrupt magnetization changes—that is, above the edges or DWs (22). By fitting the data to micromagnetic calculations (Fig. 1D), the spatial position profile  $y_{\text{DW}} = f(x)$  of the DW can be extracted with a standard error  $\approx 30$  nm in the  $y$  direction (22). Here, the DW is found to be nearly straight, with a  $3^\circ$  tilt with respect to the  $x$  axis (black line in Fig. 1B).

For an ideal magnetic sample, the DW should be straight and perpendicular to the wire axis to minimize the DW energy. However, the presence of structural or fabrication defects locally modifies the energy landscape, creating pinning sites for the DW. To occupy a local energy minimum, the DW is distorted. While repeating magnetic field measurements above the magnetic wire, we observed discrete jumps of the DW between two pinning sites, labeled 1 and 2 in Fig. 2A. The position profiles of the DW in each pinning site (Fig. 2B) reveal a spatial separation ranging from  $50 \pm 30$  nm (near the right-hand edge of the wire) to  $200 \pm 30$  nm (left-hand edge). The hopping of the DW between the two pinning sites, driven by thermal fluctuations, is known as the Barkhausen effect (23–25). Movie S1 further illustrates the observation of this effect in our experiment, performed in zero external magnetic field and at room temperature.

To analyze the dynamics of the hopping process, we monitored the magnetometer signal over time at a fixed position on the wire, above site 2 (Fig. 2A, close-up views). The resulting traces exhibit well-defined jumps between two magnetometer signal levels, reflecting DW hopping over an

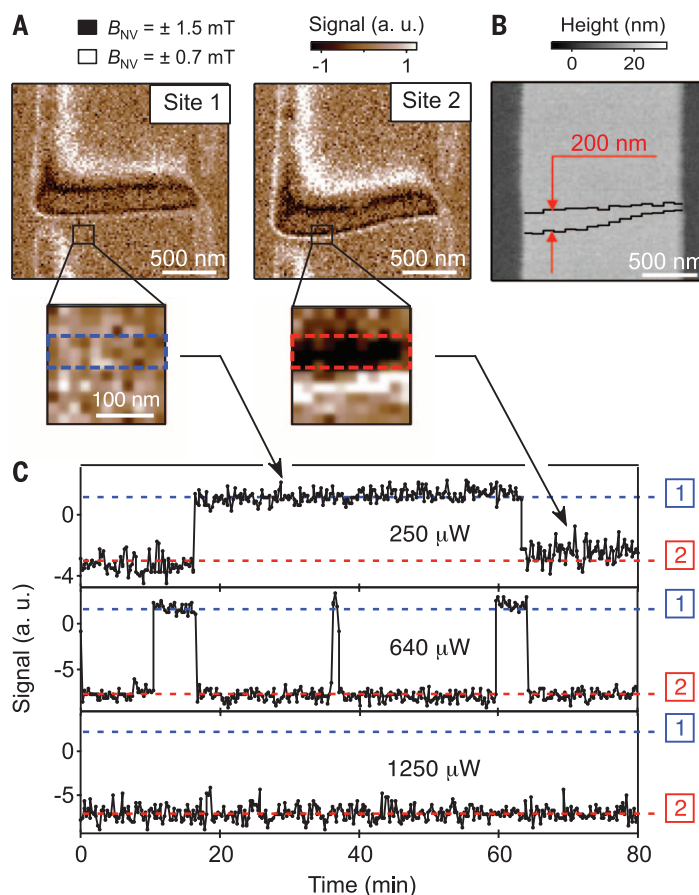
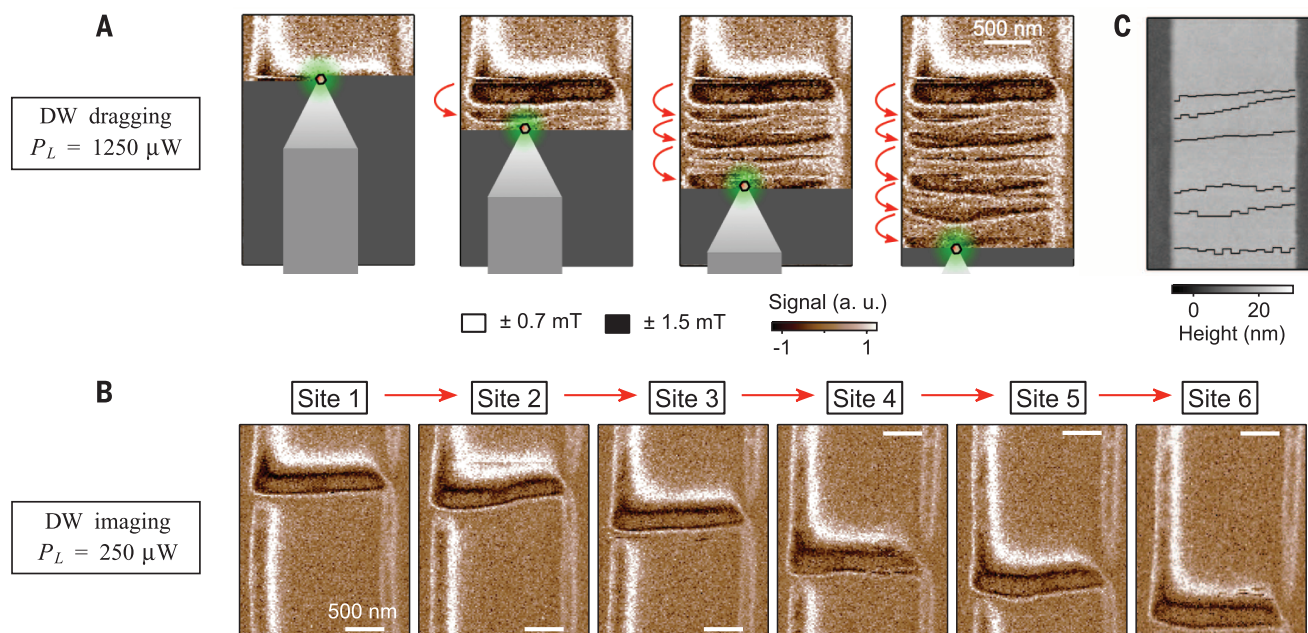
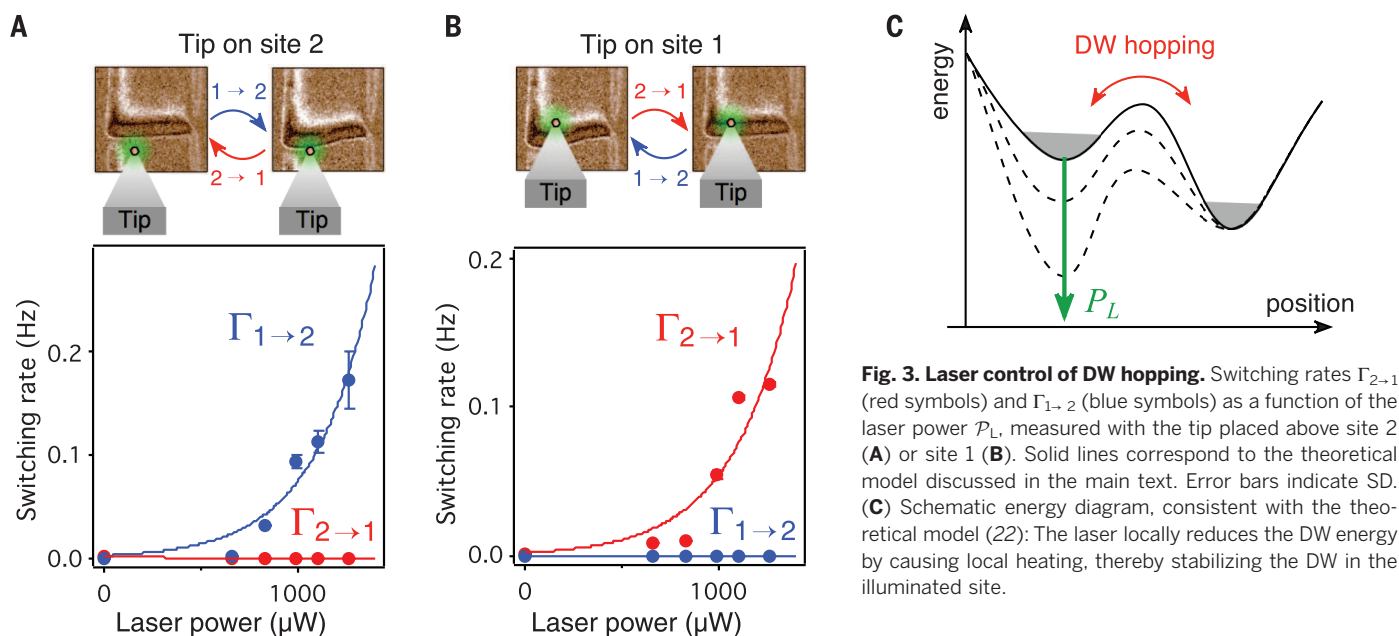


**Fig. 2. Observation of Barkhausen jumps.** (A) Dual iso-B images recorded consecutively, showing the DW in two different pinning sites, labeled 1 and 2. (B) DW position profile in each site (black lines) extracted from data fitting with micromagnetic calculations and overlaid on the AFM image. (C) Magnetometer signal traces showing DW hopping between the two pinning sites for three values of the laser power. Each data point is obtained by reducing the scanning window to the black squares shown in (A) and integrating the magnetometer signal over the dashed rectangles [see close-up views in (A)]. The acquisition time per point is 3 s.



energy barrier (Fig. 2C). Notably, the switching rates dramatically depend on the laser power  $P_L$  used to optically excite the NV defect. The lifetime of site 2 becomes substantially longer when  $P_L$  increases; at sufficiently high laser power, there are no more switching events back to site 1. The laser spot—with a diffraction-limited Gaussian profile with waist  $\approx 330 \text{ nm}$ —is focused onto the NV center probe (i.e., mostly above site 2 in these experiments), which suggests a pinning action of

the laser. Though the DW has no preferential site at low power, it is efficiently trapped into site 2 at high laser power, illustrating how laser light can be used to control DW hopping in an ultrathin magnetic wire. To get more insight into this process, the switching rates  $\Gamma_{i \rightarrow j}$  from site  $i$  to site  $j$  were measured as a function of  $P_L$  following the preparation-readout procedure described in (22). These measurements were performed with the tip (i.e., the laser spot) placed

above either site 1 or site 2 (Fig. 3, A and B). A similar behavior is observed in both cases: The switching rate toward the illuminated site increases with increasing  $P_L$ . This clearly demonstrates that the laser tends to pin the DW in the nearest available site.

This effect can be explained by laser-induced local heating, which leads to a reduction in the DW energy through the decrease in saturation magnetization and anisotropy with increasing



temperature (26, 27), as depicted in Fig. 3C. To verify this hypothesis, we developed a model of the thermally activated hopping by applying Kramer's transition rate theory to 1D stochastic DW dynamics (22). The two pinning sites are modeled as pointlike defects with an increase in the DW energy for the transition from site 1 to site 2 because of a 14-nm elongation in the wall length, as observed experimentally (Fig. 2B). The spatial profile of the laser-induced heating is assumed to mirror the Gaussian profile of the laser beam. The DW energy then acquires an additional spatial dependence as a result of this local heating, with an energy minimum at the laser spot center, which leads to an additional force that drives the DW toward this minimum. With the use of the micromagnetic parameters determined for our system from other experiments (28) and including the temperature dependence of the saturation magnetization, we find that this leads to an exponential increase in the hopping rate toward the pinning site under laser focus and confirms the intuitive picture shown in Fig. 3C. Furthermore, quantitative agreement is found with the experiment (solid lines in Fig. 3, A and B) if one assumes (i) pinning fields of 1.1 mT at site 1 and 1.8 mT at site 2, in good agreement with field-induced DW propagation measurements (29), and (ii) a temperature increase of ~6 K per milliwatt of applied power in the ferromagnetic wire at the position of the laser spot. This is in reasonable agreement with the ~20-K/mW temperature increase measured with the same NV center employed as a nanoscale thermometer (22, 30).

To explore the pinning in the wire, we then used laser-controlled hopping of the DW. By scanning the sample with a high laser power ( $P_L > 1$  mW), the DW is forced to hop toward the pinning site nearest to the tip, thereby jumping from site to site following the scan direction. Such a laser-induced DW dragging is directly observed on the magnetic field image (Fig. 4A). The DW can be efficiently prepared in a given pinning site by simply turning the laser off as soon as the DW is detected in the desired site. Following this laser-assisted preparation, the DW can be subsequently imaged with no major perturbation by using a low laser power ( $P_L = 250$   $\mu$ W). We used this dragging-imaging procedure to clearly identify six different pinning sites over the 2- $\mu$ m-long wire portion that we investigated (Fig. 4B). From the magnetic images, we inferred the DW position profiles in each site, which are overlaid on the atomic force microscopy (AFM) image in Fig. 4C. The mean spacing between consecutive stable pinning sites is ~300 nm. This is consistent with structural studies performed on such Ta/CoFeB/MgO films with x-ray diffraction (29), indicating a very low density of structural defects (interface roughness, grain boundaries, crystalline texture) with respect to other materials with perpendicular anisotropy such as Co/Pt, Co/Pd, or Co/Ni.

Our technique allows for the determination of the density of pinning sites in magnetic nanowires and for the evaluation of individual pinning

strengths in the event of a local gradient in thermal energy, two important aspects of magnetic recording applications involving magnetic DW motion and thermally assisted magnetization switching. This work also highlights the potential for NV center microscopy to manipulate micromagnetic structures at the nanoscale.

#### REFERENCES AND NOTES

1. S. S. P. Parkin, M. Hayashi, L. Thomas, *Science* **320**, 190–194 (2008).
2. M. Yamanouchi *et al.*, *Appl. Phys. Lett.* **102**, 212408 (2013).
3. A. Chanthbouala *et al.*, *Nat. Phys.* **7**, 626–630 (2011).
4. M. Hayashi, L. Thomas, R. Morya, C. Rettner, S. S. P. Parkin, *Science* **320**, 209–211 (2008).
5. S. Ikeda *et al.*, *Nat. Mater.* **9**, 721–724 (2010).
6. S. Lemerle *et al.*, *Phys. Rev. Lett.* **80**, 849–852 (1998).
7. P. J. Metaxas *et al.*, *Phys. Rev. Lett.* **99**, 217208 (2007).
8. M.-Y. Im, L. Bocklage, P. Fischer, G. Meier, *Phys. Rev. Lett.* **102**, 147204 (2009).
9. M. Kläui *et al.*, *Phys. Rev. Lett.* **95**, 026601 (2005).
10. S. Meckler *et al.*, *Phys. Rev. Lett.* **103**, 157201 (2009).
11. G. Chen *et al.*, *Phys. Rev. Lett.* **110**, 177204 (2013).
12. B. M. Chernobrod, G. P. Berman, *J. Appl. Phys.* **97**, 014903 (2005).
13. J. M. Taylor *et al.*, *Nat. Phys.* **4**, 810–816 (2008).
14. C. L. Degen, *Appl. Phys. Lett.* **92**, 243111 (2008).
15. G. Balasubramanian *et al.*, *Nature* **455**, 648–651 (2008).
16. L. Rondin *et al.*, *Rep. Prog. Phys.* **77**, 056503 (2014).
17. J. R. Maze *et al.*, *Nature* **455**, 644–647 (2008).
18. M. S. Grinolds *et al.*, *Nat. Phys.* **9**, 215–219 (2013).
19. L. Rondin *et al.*, *Nat. Commun.* **4**, 2279 (2013).
20. J.-P. Tetienne *et al.*, *Phys. Rev. B* **88**, 214408 (2013).
21. L. Rondin *et al.*, *Appl. Phys. Lett.* **100**, 153118 (2012).

22. Supplementary materials are available on Science Online.
23. A. Chizhik *et al.*, *Appl. Phys. Lett.* **97**, 012502 (2010).
24. A. Schwarz *et al.*, *Phys. Rev. Lett.* **92**, 077206 (2004).
25. J. A. J. Burgess *et al.*, *Science* **339**, 1051–1054 (2013).
26. P. Möhrke, J. Rhensius, J.-U. Thiele, L. J. Heyderman, M. Kläui, *Solid State Commun.* **150**, 489–491 (2010).
27. G. V. Astakhov *et al.*, *Phys. Rev. Lett.* **106**, 037204 (2011).
28. T. Devolder *et al.*, *Appl. Phys. Lett.* **102**, 022407 (2013).
29. C. Burrowes *et al.*, *Appl. Phys. Lett.* **103**, 182401 (2013).
30. D. M. Toyli, C. F. de las Casas, D. J. Christle, V. V. Dobrovitski, D. D. Awschalom, *Proc. Natl. Acad. Sci. U.S.A.* **110**, 8417–8421 (2013).

#### ACKNOWLEDGMENTS

We thank L. Rondin, O. Boulle, G. Gaudin, L. Vila, and B. Ocker for experimental assistance and fruitful discussions. The research has been partially funded by the European Community's Seventh Framework Programme (FP7/2007-2013) under grant agreements 611143 (DIADAMS) and 257707 (MAGWIRE); the French Agence Nationale de la Recherche through the projects DIAMAG, FRIENDS, and ELECMAGE; and C'Nano Ile-de-France (NANOMAG).

#### SUPPLEMENTARY MATERIALS

www.sciencemag.org/content/344/6190/1366/suppl/DC1  
Materials and Methods  
Supplementary Text  
Figs. S1 to S10  
Table S1  
References (31–38)  
Movie S1

23 December 2013; accepted 8 May 2014  
10.1126/science.1250113

#### NANOPHOTONICS

## Controlling graphene plasmons with resonant metal antennas and spatial conductivity patterns

P. Alonso-González,<sup>1</sup> A. Y. Nikitin,<sup>1,2</sup> F. Golmar,<sup>1,3</sup> A. Centeno,<sup>4</sup> A. Pesquera,<sup>4</sup> S. Vélez,<sup>1</sup> J. Chen,<sup>1</sup> G. Navickaite,<sup>5</sup> F. Koppens,<sup>5</sup> A. Zurutuza,<sup>4</sup> F. Casanova,<sup>1,2</sup> L. E. Hueso,<sup>1,2</sup> R. Hillenbrand<sup>2,6\*</sup>

Graphene plasmons promise unique possibilities for controlling light in nanoscale devices and for merging optics with electronics. We developed a versatile platform technology based on resonant optical antennas and conductivity patterns for launching and control of propagating graphene plasmons, an essential step for the development of graphene plasmonic circuits. We launched and focused infrared graphene plasmons with geometrically tailored antennas and observed how they refracted when passing through a two-dimensional conductivity pattern, here a prism-shaped bilayer. To that end, we directly mapped the graphene plasmon wavefronts by means of an imaging method that will be useful in testing future design concepts for nanoscale graphene plasmonic circuits and devices.

Surface plasmon polaritons—coupled excitations of photons and mobile charge carriers—in metals and doped semiconductors offer intriguing opportunities to control light in nanoscale devices (1–7). Plasmons provide both a strong local field enhancement and confinement, accompanied by an appreciable reduction of the wavelength relative to free-space radiation. However, plasmons in metals exhibit relatively strong losses and cannot be controlled by electrical fields. Con-

sequently, novel plasmonic materials are being sought (8). Among them, doped graphene is advantageous because of its two-dimensional nature

<sup>1</sup>CIC nanoGUNE, 20018 Donostia-San Sebastián, Spain.

<sup>2</sup>IKERBASQUE, Basque Foundation for Science, 48011 Bilbao, Spain. <sup>3</sup>I.N.T.I.-CONICET and ECyT-UNSAM, San Martín,

Buenos Aires, Argentina. <sup>4</sup>Graphenea SA, 20018 Donostia-San Sebastián, Spain. <sup>5</sup>ICFO-Institut de Ciències Fotòniques, Mediterranean Technology Park, 08860 Castelldefells, Barcelona, Spain. <sup>6</sup>CIC nanoGUNE and UPV/EHU, 20018 Donostia-San Sebastián, Spain.

\*Corresponding author. E-mail: r.hillenbrand@nanogune.eu